

Tomographic reconstruction of oxygen orbitals in lithium-rich battery materials

Hafiz Hasnain, Suzuki Kosuke, Barbiellini Bernardo, Tsuji Naruki, Yabuuchi Naoaki, Yamamoto Kentaro, Orikasa Yuki, Uchimoto Yoshiharu, Sakurai Yoshiharu, Sakurai Hiroshi, Bansil Arun, Viswanathan Venkatasubramanian

This is a Post-print version of a publication
published by Springer Nature
in Nature

DOI: [10.1038/s41586-021-03509-z](https://doi.org/10.1038/s41586-021-03509-z)

Copyright of the original publication:

© The Author(s), under exclusive licence to Springer Nature Limited 2021

Please cite the publication as follows:

Hafiz, H., Suzuki, K., Barbiellini, B. et al. (2021). Tomographic reconstruction of oxygen orbitals in lithium-rich battery materials. *Nature*, vol. 594. pp. 213–216. DOI: [10.1038/s41586-021-03509-z](https://doi.org/10.1038/s41586-021-03509-z)

**This is a parallel published version of an original publication.
This version can differ from the original published article.**

Tomographic reconstruction of non-bonding oxygen orbitals in Li-rich battery materials

Hasnain Hafiz^{1,†}, Kosuke Suzuki², Bernardo Barbiellini^{3,4}, Naruki Tsuji⁵, Naoaki Yabuuchi⁶, Ken-taro Yamamoto⁷, Yuki Orikasa⁸, Yoshiharu Uchimoto⁷, Yoshiharu Sakurai⁵, Hiroshi Sakurai², Arun Bansil⁴, Venkatasubramanian Viswanathan^{1,9}

¹*Department of Mechanical Engineering, Carnegie Mellon University, Pittsburgh, PA 15213, USA*

²*Faculty of Science and Technology, Gunma University, Kiryu, Gunma 376-8515, Japan*

³*School of Engineering Science, Lappeenranta University of Technology, FI-53851 Lappeenranta, Finland*

⁴*Department of Physics, Northeastern University, Boston, MA 02115, USA*

⁵*Japan Synchrotron Radiation Research Institute, SPring-8, Sayo, Hyogo 679-5198, Japan*

⁶*Department of Chemistry and Life Science, Yokohama National University, Yokohama, Kanagawa 240-8501, Japan*

⁷*Graduate School of Human and Environmental Studies, Kyoto University, Sakyo-ku, Kyoto 606-8501, Japan*

⁸*Department of Applied Chemistry, Ritsumeikan University, Kusatsu, Shiga 525-8577, Japan*

⁹*Department of Physics, Carnegie Mellon University, Pittsburgh, PA 15213, USA*

[†]*Present address: Theoretical Division, Los Alamos National Laboratory, Los Alamos, NM 87545, USA*

Electrification of heavy-duty transport and aviation requires a paradigm shift in electrode

materials and anionic redox represents one possible approach to meeting these demanding targets. However, questions on the validity of the O^{2-}/O^- oxygen redox paradigm remain open and alternative explanations for the origin of the anionic capacity have been proposed because electronic orbitals associated with redox reactions cannot be measured by standard experiments. Here, by using high energy x-ray Compton measurements along with first-principles modeling, we show how the electronic orbital that lies at the heart of the reversible and stable anionic redox activity can be imaged and visualized and its character and symmetry can be determined. Differential changes in the Compton profile with Li concentration are shown to be sensitive to the phase of the electronic wave function and carry signatures of electrostatic and covalent bonding effects. Our study not only provides a picture of the workings of a lithium-rich battery at the atomic scale but also suggests pathways for improving existing cathodes and designing new ones.

INTRODUCTION

Electrification of heavy-duty vehicles and aviation requires batteries with much higher specific energy than the current Li-ion batteries.^{1,2} Although substantial progress has been made with lithium metal anodes³ and silicon,^{4,5} there is a need to move beyond the current layered cathodes to meet these demanding targets. Li-rich oxides present a promising cathode materials class to move closer towards these targets with a high capacity of about 300 mAh/g⁶⁻¹². The anionic redox mechanism underlying their electrochemical operation, however, has been difficult to understand fully with the current probes and techniques. Experimental techniques capable of directly probing the oxy-

gen activity include x-ray photoemission spectroscopy (XPS)¹³, soft x-ray absorption (XAS)¹⁴ and x-ray resonant inelastic scattering (RIXS)¹⁵. However, the signal from the oxygen-redox reaction in the bulk sample can be masked by surface effects in these techniques. It has proven difficult to detect significant oxygen activity¹⁶ via x-ray Raman spectroscopy, even though it is more bulk sensitive.

First-principles density-functional theory (DFT) based modeling of Li-rich battery materials is sensitive to subtle correlation effects^{17,18}, and the development of robust design principles with eventual aspiration of identifying an inverse design paradigm requires an iterative and reliable experiment-theory loop at the atomic scale¹⁹. In this way, we can be in a position to undertake direct and sharpened comparisons between theoretical predictions with the corresponding experimental results in microscopic details of the cathode electronic structure to accelerate the feedback loop between theory, spectroscopy and battery design in order to identify origins of the anomalous cathode capacity.

Previous studies of cathode materials^{20,21} have demonstrated the efficacy of Compton scattering spectroscopy toward unravelling the relationship between the key battery performance characteristics and the nature of the electronic orbitals involved in Li intercalation reactions. Merits of x-ray Compton scattering over the standard techniques are enhanced penetration depth and high bulk-sensitivity, which in turn allow *in situ* and *operando* measurements of batteries^{22–25}. Since the Compton cross section²⁶ is very small even at 100 keV, radiation damage is usually negligible. X-ray Compton scattering is thus uniquely suited for probing working batteries both at the

macroscopic scale by mapping of the lithium distribution and at the atomic level by extracting characteristics of redox orbitals through tomographic reconstructions^{27,28}. An important proof point of the efficacy of the Compton scattering technique towards advancing the design rules involves high T_c cuprate superconductors, where a combined theory-experiment study provided a comprehensive understanding of the redox orbitals associated with doped holes consistent with the complex phase diagram of these strongly correlated materials²⁹.

Tracking the occupation of O 2p orbitals is crucial in solving the puzzle of Li-rich cathodes. This goal can be achieved by exploring the exemplar binary system^{8,12} of Li_2TiO_3 and LiMnO_2 given by the formula $\text{Li}_x\text{Ti}_{0.4}\text{Mn}_{0.4}\text{O}_2$ (LTMO). Here, we use high-energy x-ray Compton scattering spectra along with first-principles computations to extract the redox orbital, which stabilizes the oxidized oxygen atoms that emerge as the charging process proceeds in the LTMO cathode. We address fundamental issues regarding the nature of the key non-bonding oxygen states and the roles of Coulomb repulsion and covalent character to gain microscopic insight into the mechanisms at play in Li-rich battery materials, which are still under debate³⁰. We definitively show how anionic redox reactions in LTMO involve O ions resulting in a significant enhancement of the battery capacity. Until now, the anionic redox activity in cathode has been difficult to characterize and quantify both in experiments and simulations. We present an analysis based on x-ray Compton experiments through which we are able to quantify electrostatic repulsion and oxygen character in Li-rich cathodes. Our method is suitable for future optimization of anionic redox materials.

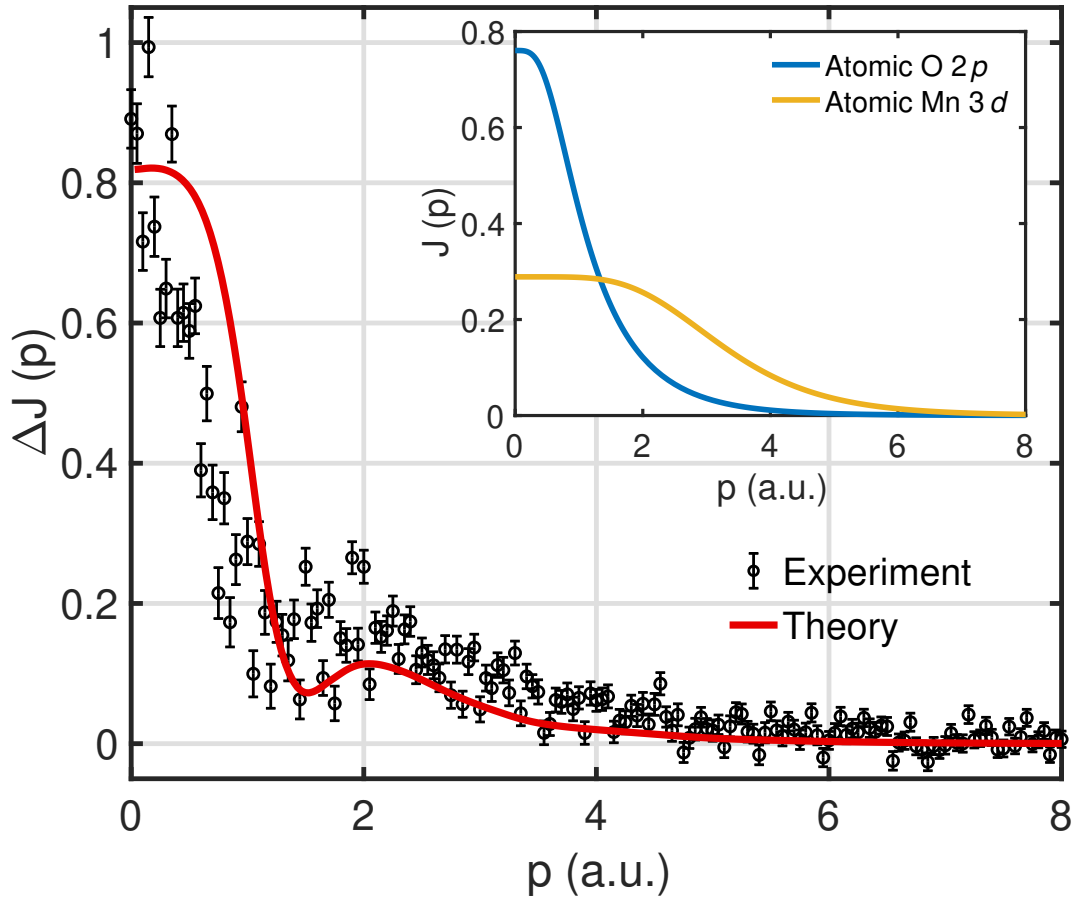


Figure 1: **Compton profile difference (CPD or ΔJ) of LTMO for Li concentration $x = 0.8$ minus $x = 0.4$.** Both experiment and theory profiles are normalized to one. The theory profile is convoluted with the experimental resolution (full-width-at-half-maximum) of 0.14 a.u. The inset shows the Compton profiles for atomic O $2p$ and Mn $3d$ orbitals.

RESULTS AND DISCUSSIONS

Compton Profile difference. Compton scattering provides a quantum mechanical description of electronic states in materials through the reconstruction of wavefunctions from experimental spectra^{26,31}. This technique is sensitive to bonding properties of materials,³² and it can detect weak bonds such as the hydrogen bond in ice and it can differentiate these bonds from purely electrostatic interactions³³. Measured Compton profiles in LTMO shown in Fig. S1 of the Supplementary Information (SI) contain features that can be used to characterize the redox orbitals²⁰. The contribution of the redox orbitals can be extracted by considering the Compton profile difference (**CPD**) between two samples with different lithium concentrations.

Figure 1 shows the CPD corresponding to the difference in profiles of $\text{Li}_x\text{Ti}_{0.4}\text{Mn}_{0.4}\text{O}_2$ for Li concentrations (x) of 0.8 and 0.4. The valence Compton profiles for the two Li concentrations are normalized here to the corresponding total number of valence electrons of the system. The area under the CPD thus gives the difference in the number of electrons for the two Li concentrations and we renormalize the CPD to one when we consider it as a projection of the momentum density of a redox orbital²⁹. This normalization to one facilitates comparison of shape of the CPD for redox orbitals in various cathode materials^{20,21,27}.

Suzuki *et al.*²⁰ observed in the spinel $\text{Li}_x\text{Mn}_2\text{O}_4$ (LMO) that the redox orbital associated with Li intercalation has mostly O 2p character. They also noticed the presence of a negative excursion between 1 and 4 a.u. in the CPD (for $x = 1.079$ and 0.496), which they accounted for in terms of transfer of some 3d electrons of Mn from localized to less localized 3d states. This

transfer induces a modulation of about 0.16 electrons in the manganese $3d$ shell. The resulting delocalization could be explained by the formation of the covalent Mn-O bond displayed in the partial density of states calculated within the DFT²⁰.

Figure 1 reveals the presence of O $2p$ anionic states in momentum space in LTMO . The long tail in the CPD can be accounted for if about 0.19 $3d$ Mn electrons are transferred from the more itinerant to less itinerant $3d$ states, see the fit in Fig. S2 in the SI. This localization is produced by the Coulomb repulsion between an occupied state at the oxygen site and the $3d$ states in the neighboring manganese ions without the formation of a significant covalent bond. Clearly, this anionic redox paradigm is different from the usual process previously examined by Suzuki *et al.*²⁰ and Barbiellini *et al.*²¹ in spinel LMO, where O $2p$ states mix with transition metal $3d$ states through the formation of the covalent bond between the oxygen and transition metal atoms. It is crucial to understand the difference between the anionic redox mechanisms in LTMO and LMO since the number of electrons, and thus the capacity, from the mixed O $2p$ and transition metal $3d$ states remains the same, independent of the oxygen character of these states. Therefore, in contrast to anionic O $2p$ redox orbitals, oxygen redox participation through bonding with a transition metal is not an effective way to increase the capacity⁷.

Our first-principles CPD model agrees well with the experiment and thus our theoretical model contains the right level of correlation effects ¹⁸ to capture the main features of the electronic structure and the corresponding electron momentum density distribution in LTMO. Clearly, the CPD highlights modifications in electron occupancy near the Fermi energy associated with lithium

insertion or extraction by eliminating contributions of irrelevant electrons²⁰. The oxygen $2p$ orbital contributes to the electron momentum density at low momenta, while the contribution of manganese $3d$ orbitals extends to high momenta as seen in the inset of Fig. 1. Note that when the Li atoms are completely ionized in the cathode material, they do not carry any valence electrons and cannot contribute to the valence Compton profile. The experimental profile is still somewhat narrower at small momenta. The reason for this is not clear but it could be due to slight delocalization of states induced by the presence of contacts between the neighboring LTMO powder grains, an effect which is not included in our simulations. Related delocalization effects have been observed in the Doppler spectra in positron annihilation studies of semiconducting nanoparticles³⁴.

We decided to measure Compton scattering profiles at $x = 0.8$ and 0.4 since we found theoretically that the energy level of the dominant oxygen state in LTMO lies around the Fermi energy and that its properties could be captured via these two Li concentrations, see Fig. S4 in SI. The partial density-of-states (PDOS) obtained from our DFT calculations for $x = 0.4$ (Fig. 2) shows the presence of a peak of a localized hole-state right above the Fermi level. These localized O $2p$ holes point in the direction of a Li atom vacancy along the Li–O–Li axis¹³. In principle, a π -type interaction exists between the O $2p$ and Mn $3d$ states¹⁰. Crystal Orbital Overlap Population (COOP) analysis shown in Fig. S5 indicates that the localized O- $2p$ states near the Fermi level involve an anti-bonding interaction with the Mn $3d$ states. However, when the Li ion fills the vacancy and the companion electron occupies the O $2p$ orbital, the π -type interaction is weak and almost non-bonding as shown by Okubo and Yamada¹⁰. Thus, the O $2p$ orbital near the Fermi level appears orphaned.

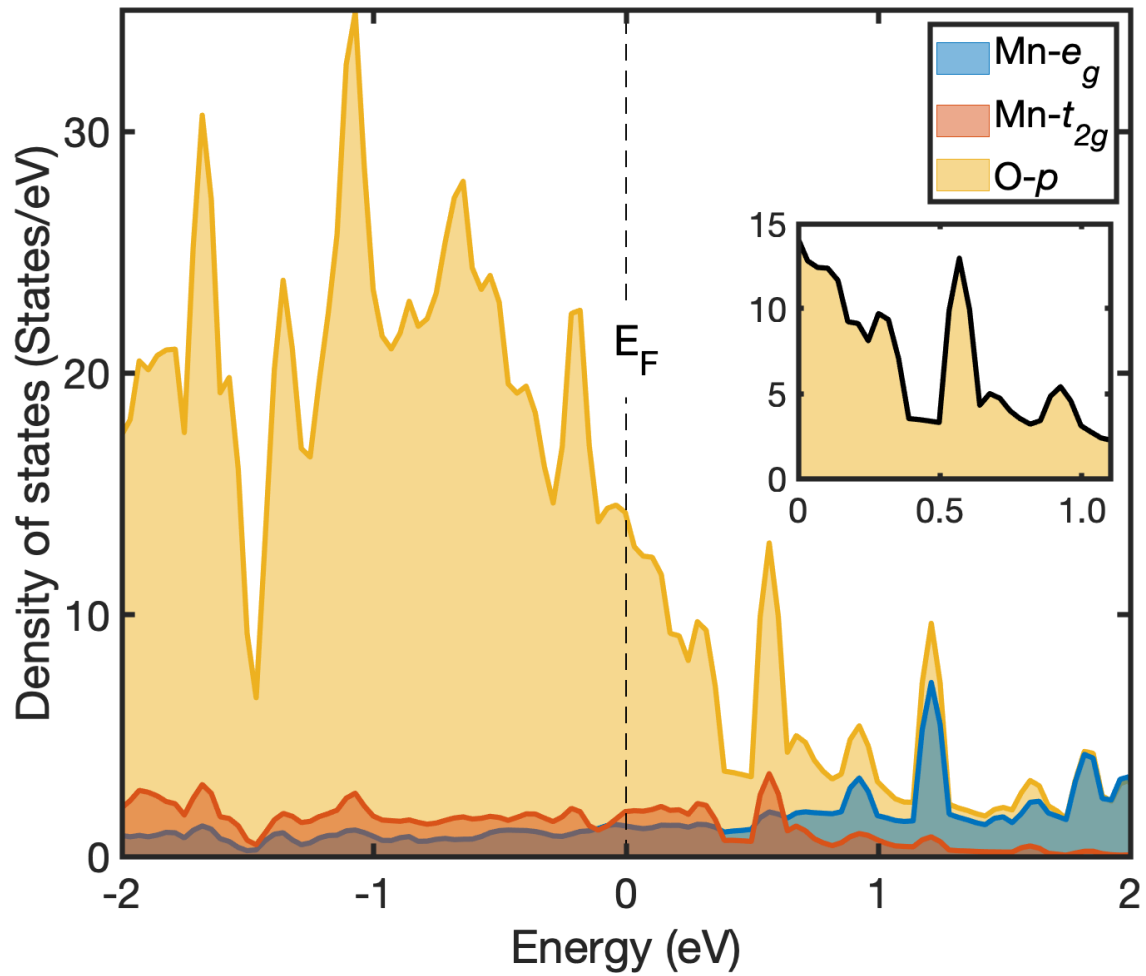


Figure 2: Partial-density-of-states (PDOS) of $\text{Li}_{0.4}\text{Ti}_{0.4}\text{Mn}_{0.4}\text{O}_2$ for the majority spin electrons near the Fermi level. PDOS associated with the Mn e_g , Mn t_{2g} and O 2p orbitals is shown. Vertical dashed line marks the Fermi energy (E_F). The inset highlights the O 2p peak.

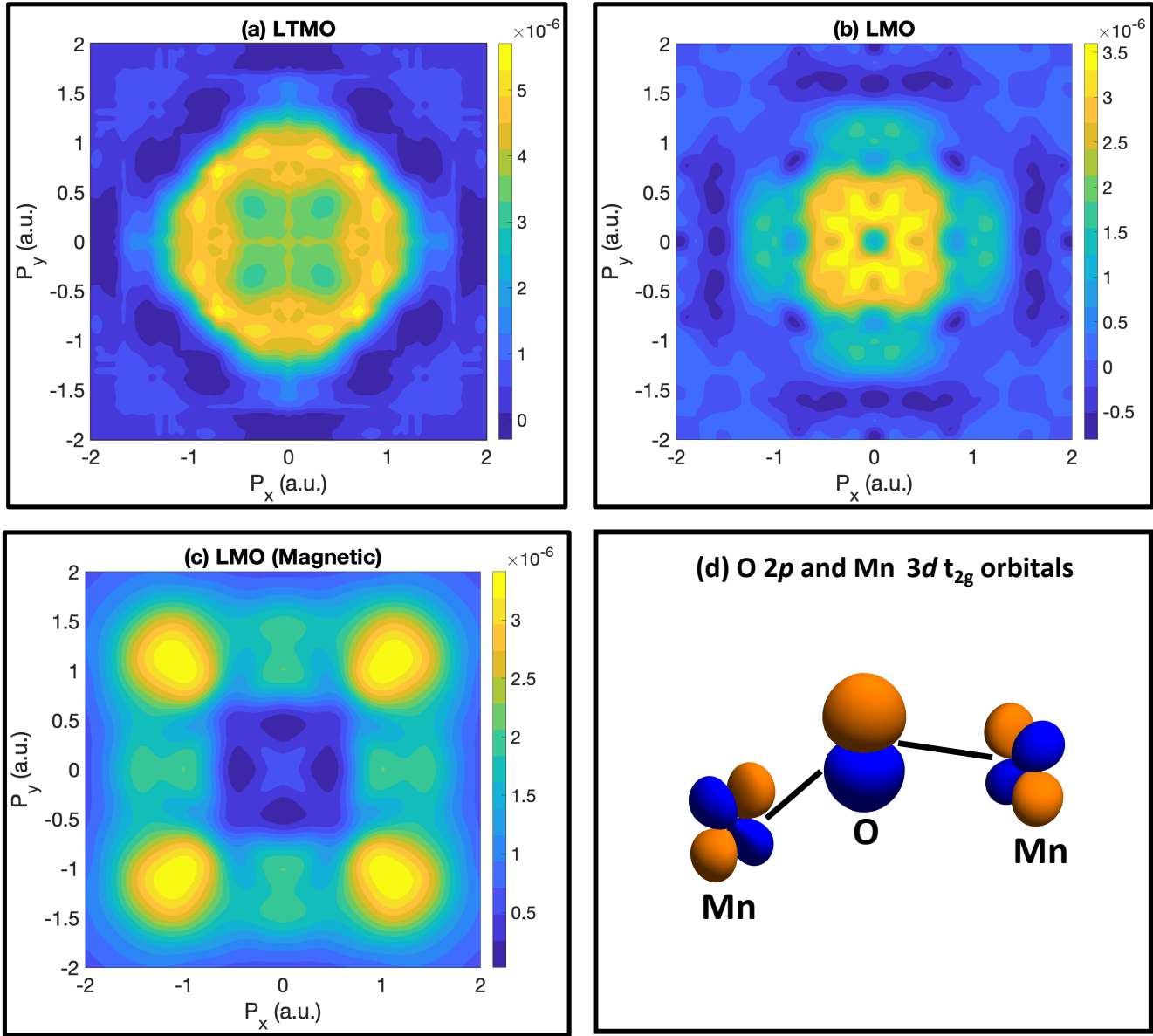


Figure 3: Reconstructed 2D electron-momentum-density (2D-EMD) maps for: (a) anionic redox orbitals in LTMO corresponding to the Li concentration between $x = 0.8$ and $x = 0.4$; (b) cationic redox orbitals in $\text{Li}_x\text{Mn}_2\text{O}_4$ corresponding to the Li concentration between $x = 1.079$ and $x = 0.496$; (c) magnetic t_{2g} orbitals in $\text{Li}_x\text{Mn}_2\text{O}_4$ extracted from magnetic Compton profile simulations²⁸; and, (d) Schematic picture of O-2p and Mn- t_{2g} orbitals. A weak π -type anti-bonding interaction exists between the O-2p and Mn- t_{2g} orbitals¹⁰.

Visualization of the anionic redox orbital. Figure 3 presents two-dimensional electron momentum densities (2D-EMDs) for the redox orbitals, which are one-dimensional integrals along a crystallographic axis of the three-dimensional EMD. These maps give information about the extent to which solid-state orbitals are modified by the chemical bonds. Experimentally, 2D-EMDs can be extracted by measuring Compton profiles for a number of different directions of the x-ray scattering vector, and the resulting spectra can be used to reconstruct the 2D-EMDs and their differences between different dopant concentration²⁹. However, in our case here the LTMO cathode is composed of a polycrystalline powder sample and, therefore, it was natural for us to base our analysis on spherically averaged experimental Compton profiles. Nevertheless, we have been able to extract the angular dependence of the redox orbital by using a careful strategy in which theoretical EMD simulations were used to model the spherically averaged experimental profile. The Bayes' theorem^{32,35} was invoked to justify this reconstruction process yielding a good fit with the experimental data, where effects of electron correlations could be varied in the modeling²⁷.

Recall that various electronic states carry their own angular characters that can be exploited for their detection. Along this line, features in Fig. 3(a) reveal the presence of repulsive Coulomb (non-bonding) interaction between the O $2p$ and Mn t_{2g} orbitals. Sharp box-like features (colored in light blue) in the high momentum region are associated with Fermi surface breaks related to the t_{2g} band. The repulsive Coulomb interaction produces a significant O- $2p$ delocalization in momentum space (or localization in real space) in comparison to the redox orbital in the spinel material $\text{Li}_x\text{Mn}_2\text{O}_4$ shown in Fig. 3(b). In the spinel case, the O $2p$ orbitals are modified by the covalent bond involving the e_g states on the Mn atoms, which induces them to localize in

momentum space (or delocalize in real space). The corresponding e_g contribution (in green color) is also more localized in the momentum space. The pure Mn t_{2g} character shown in Fig. 3(c) could be extracted by performing magnetic Compton scattering experiments²⁸. The present visualization of the repulsive Coulomb interaction between the O 2p orbital with the t_{2g} states can be used in other Li-rich cathode materials to describe the chemical hardness¹¹ of the localized non-bonding O 2p states schematized in Fig. 3(d). Displacement of the t_{2g} electrons due to Coulomb interaction produced by the occupation of the orphaned O-2p state is a key parameter to understand the origin of the voltage hysteresis^{8,11} since this quantity describes an energy penalty. Therefore, our ability to estimate this number provides a useful descriptor for understanding the working of the battery and paves the way for improving existing Li-rich materials and for designing new high-capacity cathodes.

CONCLUSION

We have provided conclusive evidence in support of the anionic redox mechanism in LTMO and rule out alternative explanations based on the Mn oxidation number. In particular, we have visualized the orphaned O-2p redox orbitals, which are responsible for achieving higher energy densities by moving beyond the limit set by the transition metal content. We have shown that the key interaction between the O 2p and Mn t_{2g} is the Coulomb repulsion, which localizes about 0.19 Mn t_{2g} electrons per Li. Therefore, because of the absence of the covalent bond in favor of Coulomb repulsion between the orphaned O-2p and Mn t_{2g} electrons, we can adduce that there is no redox involvement of Mn in LTMO over the investigated Li doping range. The visualization of the in-

teraction between the O- $2p$ and transition metal t_{2g} electrons to estimate the number of electrons displaced by the Coulomb interaction are useful descriptors for designing stable, high-capacity oxygen-redox electrode materials. Our study enables a direct visualization of orbitals involved in the anionic redox processes and offers a quantitative analyses based on new descriptors derived from the electron momentum density.

Methods

Compton experiments The Compton profile measurements were performed using a Cauchois-type x-ray spectrometer on the BL08W beamline at SPring-8 synchrotron facility (Japan)^{36–38}. Incident x-rays emitted from a multipole wiggler were used. The incident x-ray energy was tuned to 114.56 keV by a bent-type Si(400) crystal. The size of the incident x-ray beam was 2 mm square at the sample position. The sample pellet covered by the laminate film was arranged in the vacuum chamber. The scattering angle was fixed at 165 degrees. The Compton scattered x-rays, which transmitted Ge(620) spectrometer, were measured by a 2D position-sensitive detector. The raw Compton profiles were corrected for absorption, analyzer and detector efficiencies, scattering cross-section, possible double-scattering contributions and x-ray background³². Corrected Compton profiles were then normalized to the total number of valence electrons after the core electron contribution was subtracted. The core electron configurations were taken to be as follows: Li 1s, Ti 1s, 2s, 2p, 3s and 3p, Mn 1s, 2s, 2p, 3s and 3p, and O 1s and 2s. The valence electrons are estimated by subtracting core electrons from the full electronic configurations of each atoms. The overall momentum resolution in the measurements was 0.14 atomic units (a.u.) (full-width-at-half-

maximum).

Sample preparation The $\text{Li}_{1.2}\text{Ti}_{0.4}\text{Mn}_{0.4}\text{O}_2$ polycrystalline sample was prepared following the method of Yabuuchi *et al.*⁸ The starting purchased materials, Li_2CO_3 , TiO_2 (Wako Pure Chemical Industries) and Mn_2O_3 were thoroughly mixed by wet mechanical ball-milling and the mixture was heated at 900 °C for 12 hours in an inert atmosphere. Prepared $\text{Li}_{1.2}\text{Ti}_{0.4}\text{Mn}_{0.4}\text{O}_2$ powder was remixed with 10 wt.% of acetylene black using a planetary ball mill with a rotation speed at 300 rpm. In order to prepare $\text{Li}_x\text{Ti}_{0.4}\text{Mn}_{0.4}\text{O}_2$ ($x = 0, 0.4$ and 0.8), a $\text{Li}_{1.2}\text{Ti}_{0.4}\text{Mn}_{0.4}\text{O}_2$ sample was delithiated by chemical oxidation of $\text{Li}_{1.2}\text{Ti}_{0.4}\text{Mn}_{0.4}\text{O}_2$ using an oxidizing agent. The structure and lithium concentration of the obtained $\text{Li}_x\text{Ti}_{0.4}\text{Mn}_{0.4}\text{O}_2$ powder were confirmed by x-ray diffraction and inductively-coupled plasma (ICP) measurements. Synthesized $\text{Li}_x\text{Ti}_{0.4}\text{Mn}_{0.4}\text{O}_2$ pellets were covered by a laminate film to preserve vacuum conditions for Compton scattering experiment.

First-principles calculations First-principles calculations were performed using the pseudopotential projector-augmented-wave method³⁹ as implemented in the Vienna Ab-Initio Simulation Package (VASP)^{40,41}, with a kinetic energy cutoff of 600 eV for the plane-wave basis set. The exchange-correlation functional was treated within the Generalized Gradient Approximation (GGA)⁴² with a correlation correction given by the parameter $U = 5$ eV¹⁸ on the Mn-*d* orbitals, which gives results similar to those given by the recently constructed strongly-constrained-and-appropriately-normed (SCAN) meta-GGA⁴³ functional. The supercell used in LTMO calculations was $\text{Li}_{30*x}\text{Ti}_{12}\text{Mn}_{12}\text{O}_{60}$, where Li, Ti and Mn ions are randomly distributed on the cationic sites and the O ions occupy the anionic sites. The number of Li atoms in the supercell (Li_{30*x}) was adjusted with respect to Li concentrations (x). These disordered structures at different Li concentrations (x)

were generated with a Monte Carlo algorithm implemented in the Special Quasirandom Structure (SQS) code⁴⁴, which is available in the open-source ATAT toolkit⁴⁵. For energy optimization and DOS calculations, a Monkhorst-Pack k -point mesh of $3 \times 1 \times 7$ was used to sample the Brillouin zone of the supercell. The equilibrium positions of the ions were calculated via structural optimization, where the internal degrees of freedom were allowed to vary until the residual forces per atom were less than 0.05 eV/A. All calculations considered ferromagnetic ordering of the ground state with default VASP magnetic moments.

We calculated the 3D electron momentum density (EMD), $\rho(\mathbf{p})$, and the spherically averaged Compton profiles, $J(p)$, of the valence electrons from the Kohn-Sham orbitals following the method of Makkonen *et al.*⁴⁶ For this purpose, the 3D-EMD was first calculated over a dense k -point mesh to accurately captures the fine structure in the momentum density. The $J(p)$ is then obtained from the spherically averaged 3D-EMD, $\rho(\mathbf{p})$, using the formula:

$$J(p) = 2\pi \int_p^\infty \rho(p)pdp. \quad (1)$$

This scheme has been recently used to study the Compton profile of lithium iron phosphate LiFePO₄²⁷, which is as an exemplar cathode battery material.

Data availability

The data that support the findings of this study are available from the corresponding authors upon reasonable request.

Acknowledgements Authors thank Dr. Max Radin for providing feedback on the manuscript, Mr. A. Terasaka

of Gunma University for his technical support of Compton scattering experiment, and Dr. Masanobu Nakayama of Nagoya Institute of Technology for sharing his insights into COOP analysis. K.S. was supported by JSPS KAKENHI Grant Numbers JP15K17873 and JP19K05519. Compton scattering experiments were performed with the approval of JASRI (Proposals Nos. 2017A1122 and 2019B1668). The work at Northeastern University was supported by the U.S. Department of Energy, Office of Science, Basic Energy Sciences Grant No. DE-FG02-07ER46352, and benefited from Northeastern University's Advanced Scientific Computation Center (ASCC), and the allocation of time at the NERSC supercomputing center through DOE Grant No. DE-AC02-05CH11231. The work at Carnegie Mellon University was supported by the Assistant Secretary for Energy Efficiency and Renewable Energy, Office of Vehicle Technologies of the US Department of Energy (DOE) through the Advanced Battery Materials Research (BMR) Program under contract no. DE-EE0007810.

Author Contributions H.H. performed all the theoretical simulations and analyzed the data. K.S., H.S., N.T and Y.S. performed the x-ray Compton scattering experiment and data analyses. N.Y., K.Y., Y.O. and Y.U. synthesized and characterized the materials. H.H. and B.B. wrote the manuscript. V.V. and A.B. contributed to the theory, and oversaw the research and writing of the manuscript. All authors were involved in revising the manuscript.

Competing Interests The authors declare no competing interests.

Supplementary information Supplementary Information is available for this paper.

Correspondence Correspondence and requests for materials should be addressed to H.H. (Email: hafiz.h@husky.neu.edu), V.V. (Email: venkvis@cmu.edu) and A.B. (Email: ar.bansil@northeastern.edu).

References

1. Sripad, S. & Viswanathan, V. Performance metrics required of next-generation batteries to make a practical electric semi truck. *ACS Energy Lett.* **2**, 1669–1673 (2017).
2. Viswanathan, V. & Knapp, B. M. Potential for electric aircraft. *Nat. Sustain.* **2**, 88–89 (2019).
3. Krauskopf, T., Richter, F. H., Zeier, W. G. & Janek, J. Physicochemical concepts of the lithium metal anode in solid-state batteries. *Chemical Reviews* (2020).
4. Salah, M. *et al.* Pure silicon thin-film anodes for lithium-ion batteries: A review. *Journal of Power Sources* **414**, 48–67 (2019).
5. Jia, H. *et al.* Hierarchical porous silicon structures with extraordinary mechanical strength as high-performance lithium-ion battery anodes. *Nature communications* **11**, 1–9 (2020).
6. Yabuuchi, N. *et al.* High-capacity electrode materials for rechargeable lithium batteries: Li₃NbO₄-based system with cation-disordered rocksalt structure. *Proceedings of the National Academy of Sciences* **112**, 7650–7655 (2015).
7. Seo, D.-H. *et al.* The structural and chemical origin of the oxygen redox activity in layered and cation-disordered Li-excess cathode materials. *Nature chemistry* **8**, 692 (2016).
8. Yabuuchi, N. *et al.* Origin of stabilization and destabilization in solid-state redox reaction of oxide ions for lithium-ion batteries. *Nature communications* **7**, 1–10 (2016).

9. Li, B. & Xia, D. Anionic redox in rechargeable lithium batteries. *Advanced Materials* **29**, 1701054 (2017).
10. Okubo, M. & Yamada, A. Molecular orbital principles of oxygen-redox battery electrodes. *ACS applied materials & interfaces* **9**, 36463–36472 (2017).
11. Assat, G. & Tarascon, J.-M. Fundamental understanding and practical challenges of anionic redox activity in Li-ion batteries. *Nature Energy* **3**, 373–386 (2018).
12. Clément, R., Lun, Z. & Ceder, G. Cation-disordered rocksalt transition metal oxides and oxyfluorides for high energy lithium-ion cathodes. *Energy & Environmental Science* **13**, 345–373 (2020).
13. Naylor, A. J. *et al.* Depth-dependent oxygen redox activity in lithium-rich layered oxide cathodes. *Journal of Materials Chemistry A* **7**, 25355–25368 (2019).
14. Li, M. *et al.* Cationic and anionic redox in lithium-ion based batteries. *Chemical Society Reviews* **49**, 1688–1705 (2020).
15. Xu, J. *et al.* Elucidating anionic oxygen activity in lithium-rich layered oxides. *Nature communications* **9**, 1–10 (2018).
16. Mukai, K., Nonaka, T., Uyama, T. & Nishimura, Y. F. In situ x-ray Raman spectroscopy and magnetic susceptibility study on Li [Li_{0.15}Mn_{1.85}] O₄ oxygen anion redox reaction. *Chemical Communications* (2020).

17. Hong, J. *et al.* Metal–oxygen decoordination stabilizes anion redox in Li-rich oxides. *Nature Materials* **18**, 256–265 (2019).
18. Tygesen, A. S., Chang, J. H., Vegge, T. & García-Lastra, J. M. Computational framework for a systematic investigation of anionic redox process in Li-rich compounds. *npj Computational Materials* **6**, 1–9 (2020).
19. Bhowmik, A. *et al.* A perspective on inverse design of battery interphases using multi-scale modelling, experiments and generative deep learning. *Energy Storage Materials* **21**, 446–456 (2019).
20. Suzuki, K. *et al.* Extracting the redox orbitals in Li battery materials with high-resolution x-ray Compton scattering spectroscopy. *Phys. Rev. Lett.* **114**, 087401 (2015).
21. Barbiellini, B. *et al.* Identifying a descriptor for *d*-orbital delocalization in cathodes of Li batteries based on x-ray Compton scattering. *Applied Physics Letters* **109**, 073102 (2016).
22. Suzuki, K. *et al.* Non-destructive measurement of *in-operando* lithium concentration in batteries via x-ray Compton scattering. *Journal of Applied Physics* **119**, 025103 (2016).
23. Suzuki, K. *et al.* *In operando* quantitation of Li concentration for a commercial Li-ion rechargeable battery using high-energy x-ray Compton scattering. *Journal of synchrotron radiation* **24**, 1006–1011 (2017).
24. Suzuki, K. *et al.* Dependency of the charge-discharge rate on lithium reaction distributions for a commercial lithium coin cell visualized by Compton scattering imaging. *Condensed Matter* **3**, 27 (2018).

25. Suzuki, K. *et al.* High-energy x-ray Compton scattering imaging of 18650-type lithium-ion battery cell. *Condensed Matter* **4**, 66 (2019).
26. Kaplan, I., Barbiellini, B. & Bansil, A. Compton scattering beyond the impulse approximation. *Physical Review B* **68**, 235104 (2003).
27. Hafiz, H. *et al.* Visualizing redox orbitals and their potentials in advanced lithium-ion battery materials using high-resolution x-ray Compton scattering. *Science advances* **3**, e1700971 (2017).
28. Hafiz, H. *et al.* Identification of ferrimagnetic orbitals preventing spinel degradation by charge ordering in $\text{Li}_x\text{Mn}_2\text{O}_4$. *Physical Review B* **100**, 205104 (2019).
29. Sakurai, Y. *et al.* Imaging doped holes in a cuprate superconductor with high-resolution Compton scattering. *Science* **332**, 698–702 (2011).
30. Radin, M. D., Vinckeviciute, J., Seshadri, R. & Van der Ven, A. Manganese oxidation as the origin of the anomalous capacity of Mn-containing Li-excess cathode materials. *Nature Energy* **4**, 639–646 (2019).
31. Schwarz, W. E. Measuring orbitals: provocation or reality? *Angewandte Chemie International Edition* **45**, 1508–1517 (2006).
32. Cooper, M. *et al.* *X-ray Compton scattering* (Oxford University Press on Demand, 2004).
33. Isaacs, E. *et al.* Covalency of the hydrogen bond in ice: A direct x-ray measurement. *Physical Review Letters* **82**, 600 (1999).

34. Eijt, S. W. H. *et al.* Electronic coupling of colloidal CdSe nanocrystals monitored by thin-film positron-electron momentum density methods. *Applied Physics Letters* **94**, 091908 (2009).
35. Hoffmann, L., Shukla, A., Peter, M., Barbiellini, B. & Manuel, A. Linear and non-linear approaches to solve the inverse problem: applications to positron annihilation experiments. *Nuclear Instruments and Methods in Physics Research Section A: Accelerators, Spectrometers, Detectors and Associated Equipment* **335**, 276–287 (1993).
36. Hiraoka, N. *et al.* A new x-ray spectrometer for high-resolution Compton profile measurements at Spring-8. *Journal of synchrotron radiation* **8**, 26–32 (2001).
37. Itou, M. *et al.* Present status of the Cauchois-type Compton scattering spectrometer at Spring-8. *Nuclear Instruments and Methods in Physics Research Section A: Accelerators, Spectrometers, Detectors and Associated Equipment* **467**, 1109–1112 (2001).
38. Sakurai, Y. & Itou, M. A Cauchois-type x-ray spectrometer for momentum density studies on heavy-element materials. *Journal of Physics and Chemistry of Solids* **65**, 2061–2064 (2004).
39. Kresse, G. & Joubert, D. From ultrasoft pseudopotentials to the projector augmented-wave method. *Phys. Rev. B* **59**, 1758–1775 (1999).
40. Kresse, G. & Furthmüller, J. Efficiency of *ab-initio* total energy calculations for metals and semiconductors using a plane-wave basis set. *Comput. Mater. Sci.* **6**, 15 – 50 (1996).
41. Kresse, G. & Furthmüller, J. Efficient iterative schemes for *ab initio* total-energy calculations using a plane-wave basis set. *Phys. Rev. B* **54**, 11169–11186 (1996).

42. Perdew, J. P., Burke, K. & Ernzerhof, M. Generalized gradient approximation made simple. *Phys. Rev. Lett.* **77**, 3865–3868 (1996).
43. Sun, J., Ruzsinszky, A. & Perdew, J. P. Strongly constrained and appropriately normed semilocal density functional. *Phys. Rev. Lett.* **115**, 036402 (2015).
44. Walle, A. v. d. *et al.* Efficient stochastic generation of special quasirandom structures. *Calphad* **42**, 13–18 (2013).
45. Walle, A. v. d., Asta, M. & M. Asta, G., Ceder. The alloy theoretic automated toolkit: a user guide. *Calphad Journal* **26**, 539–553 (2002).
46. Makkonen, I., Hakala, M. & Puska, M. Calculation of valence electron momentum densities using the projector augmented-wave method. *Journal of Physics and Chemistry of Solids* **66**, 1128–1135 (2005).

Supplementary Information: Tomographic reconstruction of oxygen orbitals in Li-rich battery materials

Hasnain Hafiz¹, Kosuke Suzuki², Bernardo Barbiellini^{3,4}, Naruki Tsuji⁵, Naoaki Yabuuchi⁶, Ken-taro Yamamoto⁷, Yuki Orikasa⁸, Yoshiharu Uchimoto⁷, Yoshiharu Sakurai⁵, Hiroshi Sakurai², Arun Bansil⁴, Venkatasubramanian Viswanathan^{1,9}

¹*Department of Mechanical Engineering, Carnegie Mellon University, Pittsburgh, PA 15213, USA*

²*Faculty of Science and Technology, Gunma University, Kiryu, Gunma 376-8515, Japan*

³*School of Engineering Science, Lappeenranta University of Technology, FI-53851 Lappeenranta, Finland*

⁴*Department of Physics, Northeastern University, Boston, MA 02115, USA*

⁵*Japan Synchrotron Radiation Research Institute, SPring-8, Sayo, Hyogo 679-5198, Japan*

⁶*Department of Chemistry and Life Science, Yokohama National University, Yokohama, Kanagawa 240-8501, Japan*

⁷*Graduate School of Human and Environmental Studies, Kyoto University, Sakyo-ku, Kyoto 606-8501, Japan*

⁸*Department of Applied Chemistry, Ritsumeikan University, Kusatsu, Shiga 525-8577, Japan*

⁹*Department of Physics, Carnegie Mellon University, Pittsburgh, PA 15213, USA*

[†]*Present address: Theoretical Division, Los Alamos National Laboratory, Los Alamos, New Mexico 87545, USA*

1 Experimental Compton profiles

The experimental Compton profiles shown in Fig. S1 code the information about various occupied electronic orbitals in the material through their electronic momentum distributions (EMDs) [1]. A spherically averaged Compton profile is related to a spherical average of the EMD as given in Eq. 1 in the Methods section. Figure S1 shows that the width of the Compton profile narrows with lithium concentration. Therefore, measures of this width can be used to estimate the state of charge of cathode as shown by Suzuki *et al.* [2]

2 Atomic orbital Compton profiles and fitting curves

Figure S2 shows our curve fitting analysis of the Compton profile difference (CPD). This analysis is based on using three distinct model profiles: an atomic Li-2s Compton profile[3], an atomic O-2p Compton profile [3, 4] and a Compton profile modulation, called the Coulomb profile, which accounts for effects of 3d orbital localization in real space due to Coulomb interaction at Mn sites [5]. The combinations of these model profiles results in the fitting curve (red line). The atomic Compton profiles are calculated using the radial wavefunctions defined by Slater orbitals [6], which are characterized by an effective exponent Z_{eff} . For example, the Slater type orbitals of xy symmetry is given by, $\psi_{xy} = Nxye^{-Z_{eff}r}$, where N is the normalization factor. We allowed variational freedom to Z_{eff} in optimizing the fit. For the Mn 3d orbital, values of Z_{eff} (4.3 and 3.0) have been chosen to reproduce the shape of the experimentally observed long tail in the CPD. Mn 3d orbital Compton profiles corresponding to these Z_{eff} values are shown in the inset of Fig. S2.

Mn 3d Compton profile for $Z_{eff} = 4.3$ (green curve in Fig. S2 inset) is more localized in real space (less localized in momentum space) than that for $Z_{eff} = 3$ (purple curve in Fig. S2 inset) and their difference gives the Coulomb profile (yellow line in Fig. S2).

The fitting procedure for the Mn 3d orbital localization is further justified by an analysis of reciprocal form factor [7], $B(r)$, which is the Fourier transform of the CPD. The experimental and fitted $B(r)$ shapes agree very well over distances near the origin corresponding to the range of the 3d orbitals as shown in Fig. S3. We also estimate the $B(r)$ for the experimental Coulomb profile by subtracting $B(r)$ of the atomic O 2p orbital from the experimental $B(r)$. This procedure allows us to determine an exponent for the O 2p orbital ($Z_{eff} = 2.12$) by minimizing the distance between the experimental Coulomb profile $B(r)$ (black dashed line in Fig. S3) and the $B(r)$ contributions of the model Coulomb profile (yellow line in Fig. S3). Note that both Mn and O are embedded in the cathode material. The modification of the exponent Z_{eff} for the 3d orbitals is an effective way to mimic the mechanism proposed by Okubo and Yamada [8]. In this mechanism, Coulomb correlation effects related to the occupation of O 2p states leads an increase of the Z_{eff} for the Mn 3d electrons involved in a π -type interaction. Consequently, two values of Z_{eff} can coexist in the Mn 3d shell of LTMO.

In order to check the extent to which the Li-2s orbital contributes to the CPD, we have carried out a Bader charge analysis [9] by taking the $x = 0.8$ LTMO as an example and found that no more than 1.2% of 2s electrons remain on Li atoms in this case, indicating that the Li atoms are essentially fully ionized. This small Li-2s character ($Z_{eff} = 1.28$) marginally contributes to the

fitting curve below 1 a.u. as seen from the cyan colored curve in Fig. S2.

The fitted curve shows the presence of a concave structure (dip) around 1.5 a.u. in the CPD in Fig. S2. We attribute this dip feature as originating from the localization of Mn 3d states. The reason is that the model Coulomb profile (yellow line in Fig. S2) is rather flat up to about 1 a.u. and it begins to develop a slope starting around 1.5 a.u. When the Coulomb profile is combined with the atomic O-2p Compton profile (blue line in Fig. S2), we obtain the dip feature around 1.5 a.u in the total profile (red curve in Fig. S2). Moreover, since the Coulomb profile is a modulation in momentum space produced by Coulomb repulsion between the electrons, it contributes to the long tail in the CPD. This modulation integrates to zero but its absolute value is two times the number of electrons displaced via Coulomb repulsion in the presence of an electron occupying the O 2p orbital, where the CPD is normalized to one.

3 Partial density of states (PDOS) and Crystal Orbital Overlap Population (COOP) analysis

Importance of the O 2p orbital can be seen with reference to the PDOS in Fig. S4. The O 2p orbital for Li concentration $x = 0.4$ lies above the Fermi level as discussed in the main text, while for $x = 0.8$ this orbital is located below the Fermi energy. Since Compton profile only includes the momentum density of occupied electrons, the CPD codes the difference in the occupation of the O 2p orbital between $x = 0.8$ minus $x = 0.4$. Contribution of the O 2p orbital to the CPD then follows immediately from the dominant O 2p character of the PDOS. The COOP analysis of the

O 2p orbital of $x = 0.4$, shown in Fig. S5, confirms the anti-bonding character of this orbital in terms of π -type interaction with Mn t_{2g} orbitals, which is in agreement with the results of Okubo and Yamada [8]. COOP analysis was carried out using the Local Orbital Basis Suite Towards Electronic-Structure Reconstruction (LOBSTER) program [10].

4 Connection between experimental CPD and the reconstructed 2D-EMD maps of redox orbitals

Figure S6 shows the connection between the experimental CPD shown in Fig. 1 to the 2D-EMD maps of redox orbitals shown in Fig. 3a. To make this connection, one can use the following procedure. First, one fits the experimental data to a model in order to remove the noise. In our case, this model is the calculated spherical average CPD (red curve) shown in Fig. 1. Second, the spherical averaged electron momentum density (EMD) is extracted using the inverse formula;

$$\rho(p) = -\frac{1}{2\pi p} \frac{dJ}{dp}. \quad (1)$$

Then, in this context, the Bayes theorem can be invoked to connect the simulations to the experimental results as explained in detail in Ref [11]. Therefore, we see that the spherical averaged EMD shown in Fig. S6 is consistent with the 2D-EMD of Fig. 3a. Notably, in both figures we observe a strong peak located at 1 a.u.

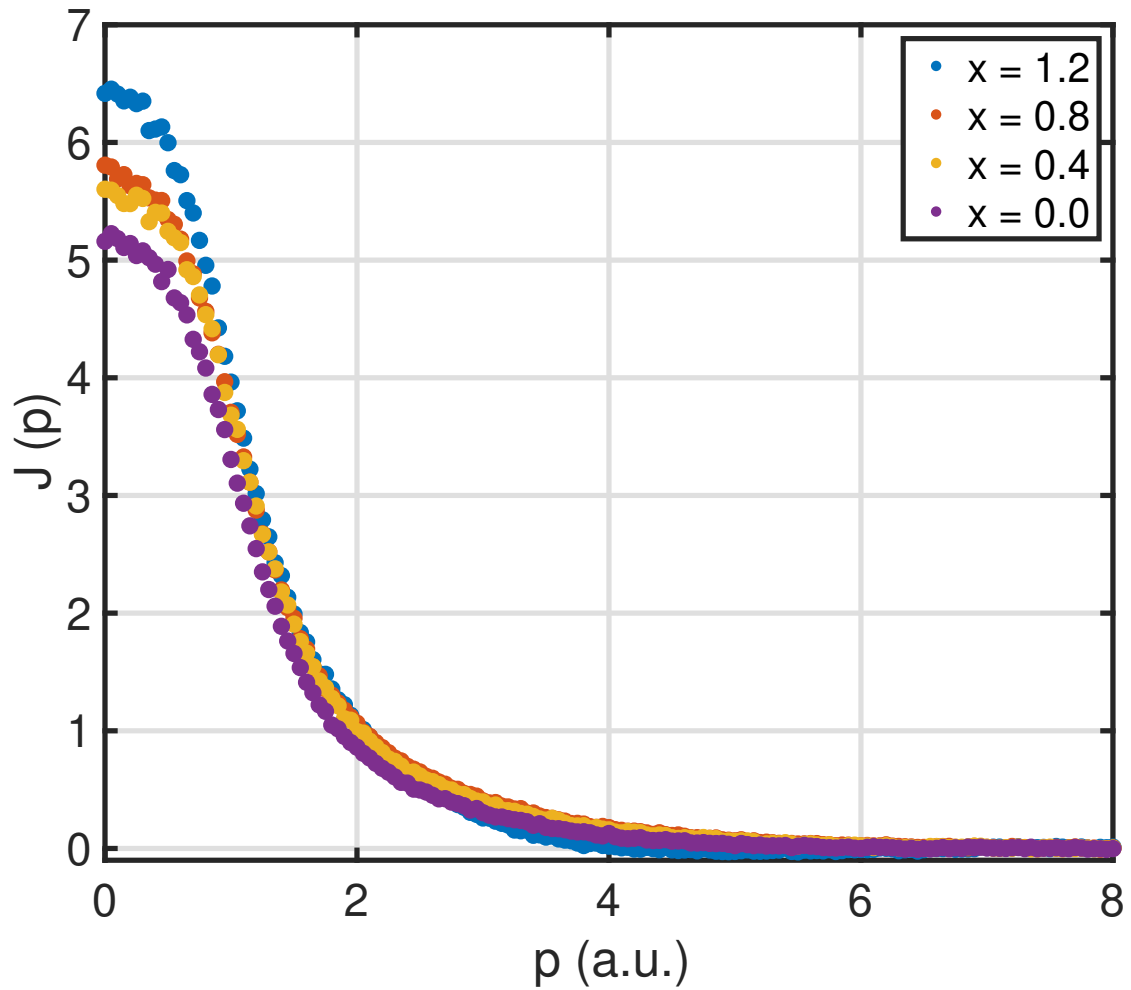


Figure S1: Experimental Compton profiles of $\text{Li}_x\text{Ti}_{0.4}\text{Mn}_{0.4}\text{O}_2$ for various Li concentrations as given in the legend.

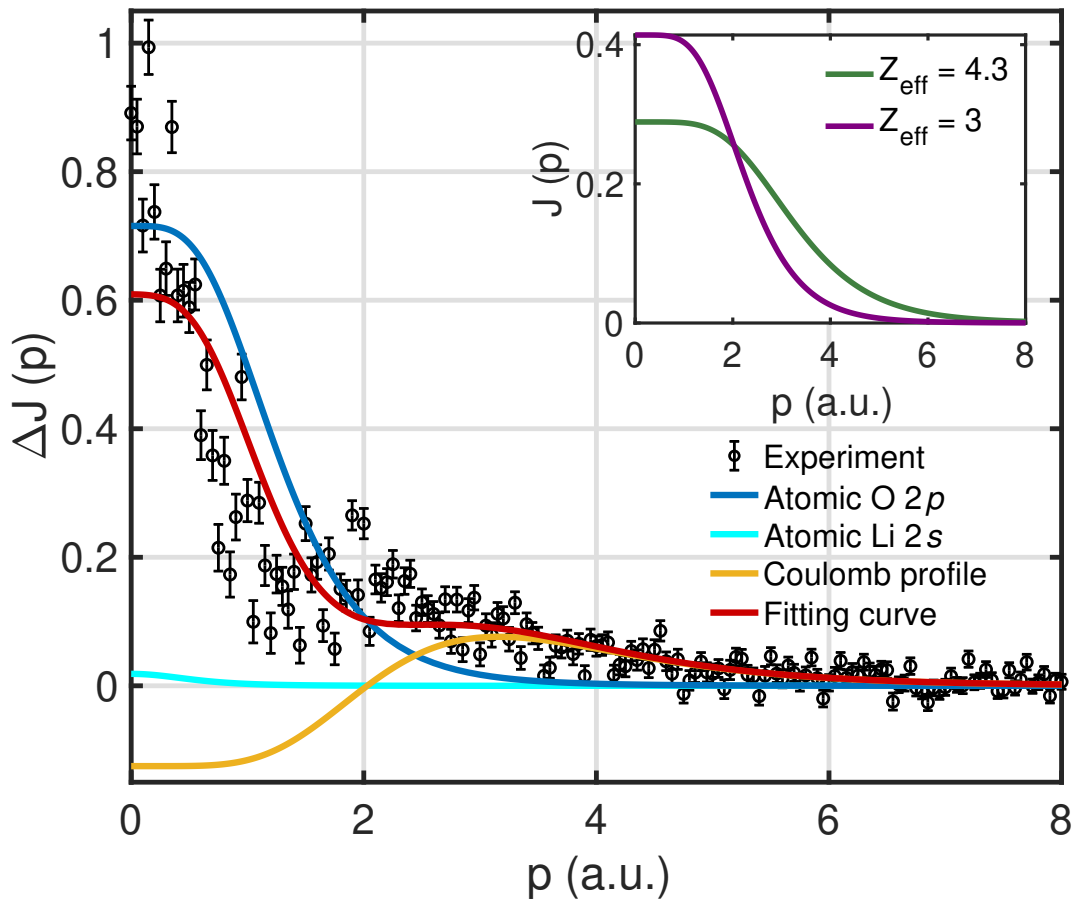


Figure S2: Comparison of experimental Compton profile difference (CPDs, denoted by ΔJ) in LTMO with theoretical models and fits. Blue line gives result of linear combination of atomic O 2p orbitals, cyan line represents the atomic Li 2s orbitals and the yellow line is for a model Coulomb repulsion profile of Mn 3d orbitals discussed in the text. The experimental CPD is the difference of Compton profiles for Li concentrations $x = 0.8$ minus $x = 0.4$. The Coulomb repulsion profile (yellow line) is obtained analytically to take into account the effects of localization of the atomic Mn 3d orbitals using normalized Slater-type orbitals. The inset shows Mn 3d Compton profiles for two different effective values of Z_{eff} . The fitting curve and ΔJ are both normalized to one.

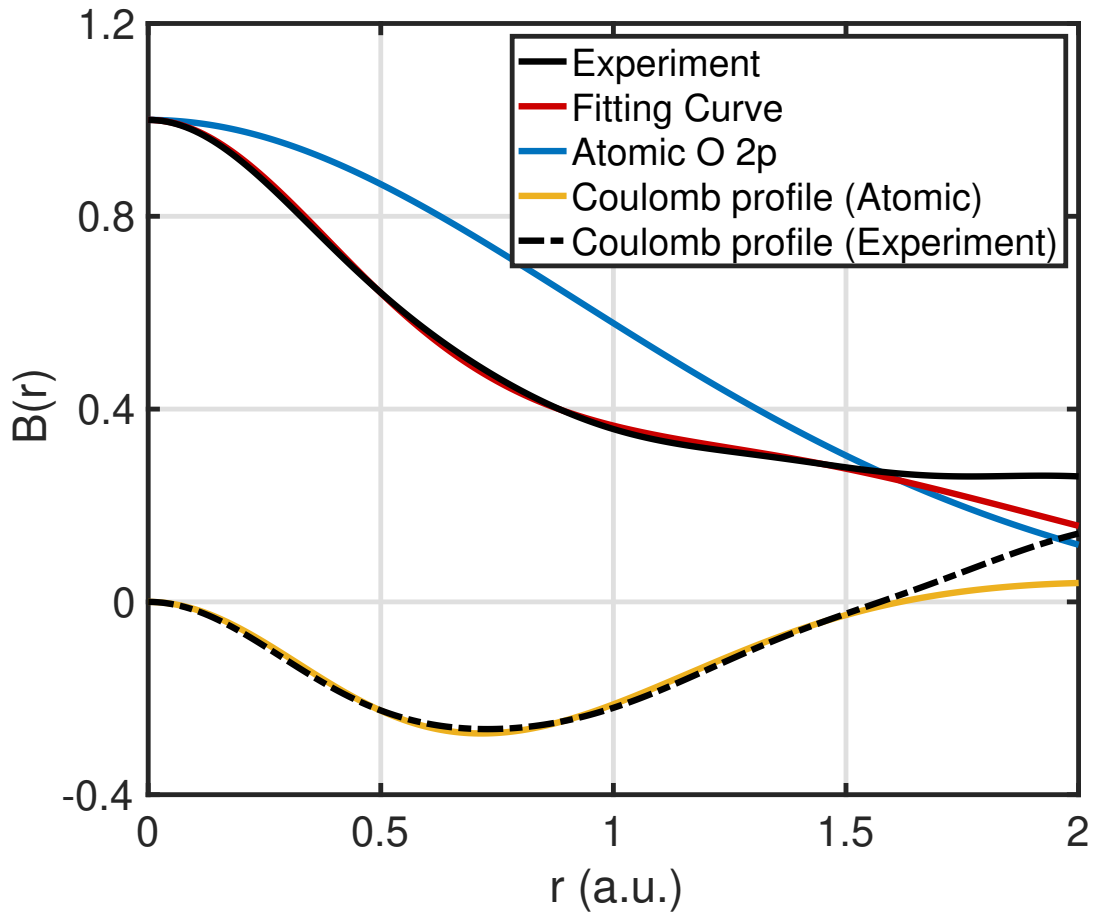


Figure S3: Fourier transform $B(r)$ of the CPD. The reciprocal form factor $B(r)$ computed for the CPD (black solid line), the fitted curve (red line) and the Coulomb profile (yellow line) shown in Fig. S2. $B(r)$ for experimental Coulomb profile (black dashed-line) is obtained by subtracting $B(r)$ of atomic O 2p (blue line) from the experimental $B(r)$ (black solid line). Agreement between fitted $B(r)$ (red line) and experimental $B(r)$ (black solid line) was used to assess the goodness of the fit of Fig. S2 (red line).

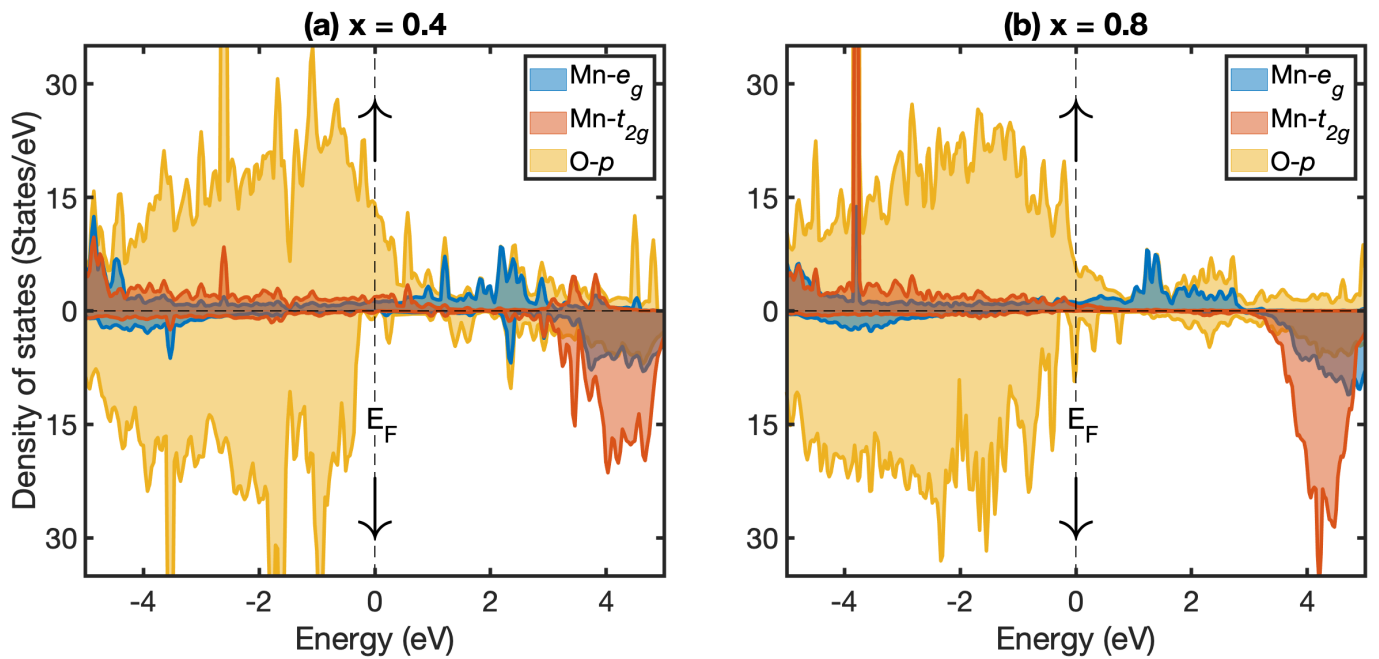


Figure S4: Spin-dependent partial density of states (PDOS) associated with Mn e_g , Mn t_{2g} and O p orbitals in $\text{Li}_x\text{Ti}_{0.4}\text{Mn}_{0.4}\text{O}_2$ for Li concentrations (a) $x = 0.4$ and (b) $x = 0.8$. Vertical dashed-line marks the Fermi energy (E_F). Up and down arrows indicate the contributions of spin-up and spin-down contributions to the PDOS, respectively.

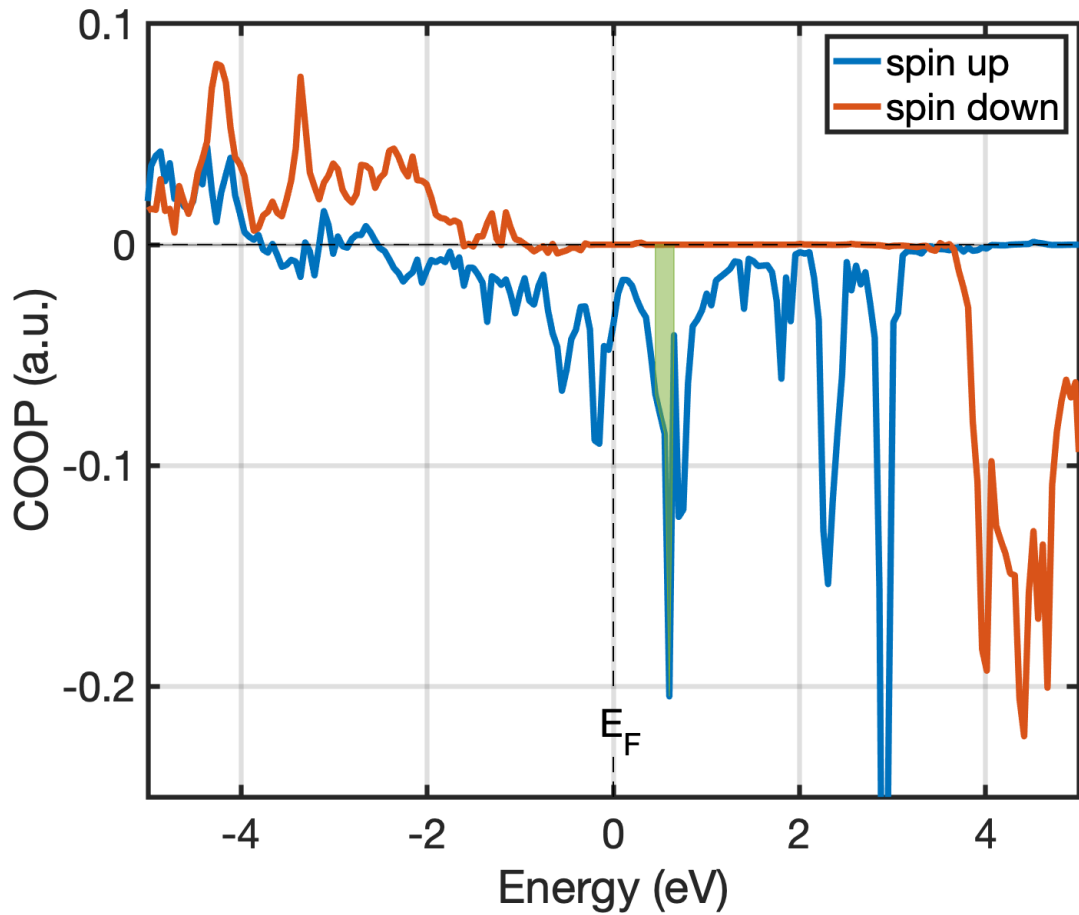


Figure S5: Crystal Orbital Overlap Population (COOP) analysis between O 2p and Mn 3d states for Li concentration $x = 0.4$. Vertical dashed-line marks the Fermi energy (E_F). COOP analysis indicates an antibonding character (green shaded area) for localized O 2p states right above the Fermi level as shown in the PDOS in Fig. 2 of the main text and Fig. S4(a). Here, localized O 2p holes point in the direction of a Li atom vacancy along the direction of the Li–O–Li axis.

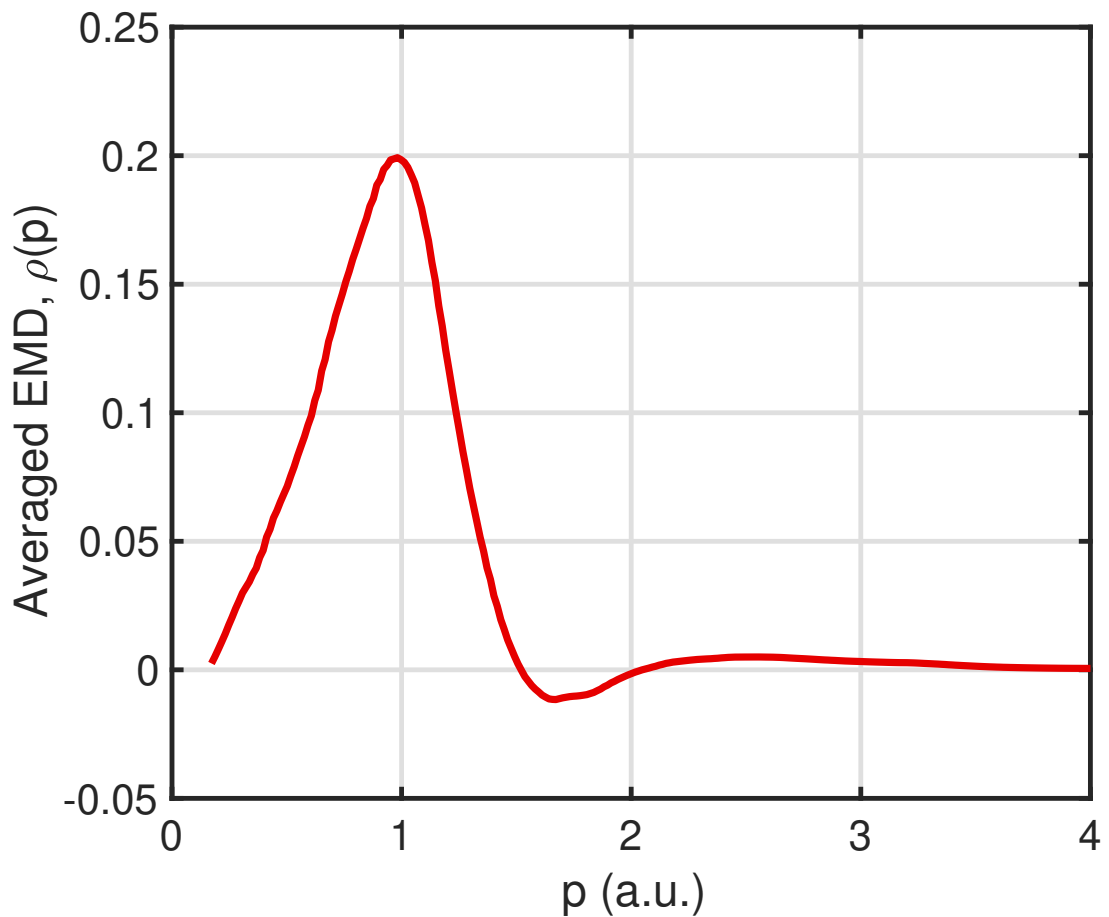


Figure S6: **Spherical averaged EMD, $\rho(p)$.** The EMD values are calculated using the formula in Equation 1 in the supplementary information. Since the factor $1/p$ diverges at low momenta, we disregard points near the origin.

References

1. Kaplan, I., Barbiellini, B. & Bansil, A. Compton scattering beyond the impulse approximation. *Physical Review B* **68**, 235104 (2003).
2. Suzuki, K. *et al.* Non-destructive measurement of in-operando lithium concentration in batteries via x-ray compton scattering. *Journal of Applied Physics* **119**, 025103 (2016).
3. Duncanson, W. & Coulson, C. Theoretical shape of the compton profile for atoms from h to ne. *Proceedings of the Physical Society* **57**, 190 (1945).
4. Biggs, F., Mendelsohn, L. & Mann, J. Hartree-fock compton profiles for the elements. *Atomic data and nuclear data tables* **16**, 201–309 (1975).
5. Kaijser, P. & Smith Jr, V. H. Evaluation of momentum distributions and compton profiles for atomic and molecular systems. In *Advances in quantum chemistry*, vol. 10, 37–76 (Elsevier, 1977).
6. Slater, J. C. Atomic shielding constants. *Phys. Rev.* **36**, 57–64 (1930).
7. Weyrich, W., Pattison, P. & Williams, B. Fourier analysis of the compton profile: atoms and molecules. *Chemical Physics* **41**, 271–284 (1979).
8. Okubo, M. & Yamada, A. Molecular orbital principles of oxygen-redox battery electrodes. *ACS applied materials & interfaces* **9**, 36463–36472 (2017).

9. Yu, M. & Trinkle, D. R. Accurate and efficient algorithm for bader charge integration. *The Journal of chemical physics* **134**, 064111 (2011).
10. Maintz, S., Deringer, V. L., Tchougréeff, A. L. & Dronskowski, R. Lobster: A tool to extract chemical bonding from plane-wave based dft. *Journal of computational chemistry* **37**, 1030–1035 (2016).
11. Dobrzański, L. Momentum density studies by the maximum entropy method. *Cooper MJ et al* 188–209 (2004).